

ARTICLE OPEN



Radiative forcing bias calculation based on COSMO (Core-Shell Mie model Optimization) and AERONET data

Pravash Tiwari¹, Jason Blake Cohen¹[✉], Xinying Wang², Shuo Wang^{1,3} and Kai Qin¹

Direct radiative forcing (DRF) of aerosols is driven by aerosol concentration, size, and mixing state, and solar radiation. This work introduces Core-Shell Mie model optimization (COSMO) to compute top of the atmosphere (TOA) forcing based on inversely constrained black carbon (BC) size and mixing state from AERONET, over two rapidly developing areas: Lumbini and Taihu. COSMO has both, a less negative TOA than AERONET and a wider range of variability, with the mean and standard deviation difference between COSMO and AERONET being $13 \pm 8.1 \text{ W m}^{-2}$ at Lumbini and $16 \pm 12 \text{ W m}^{-2}$ at Taihu. These differences are driven by particle aging and size-resolved BC emissions, with up to 17.9% of cases warmer than the maximum AERONET TOA, and 1.9% of the total possible cases show a net-warming at TOA ($\text{TOA} > 0$). A linearized correction is deduced which can be immediately implemented by climate models, and suggested ranges of BC size and mixing observations are made for future campaigns. Given that the COSMO TOA bias and uncertainty are larger than the forcing of locally emitted GHGs, active consideration of BC is necessary to reduce climate uncertainty in developing areas.

npj Climate and Atmospheric Science (2023)6:193; <https://doi.org/10.1038/s41612-023-00520-1>

INTRODUCTION

Submicron sized carbon-containing aerosols black carbon (BC) and brown carbon (BrC) (herein called absorbing aerosols (AA)) are emitted due to the incomplete combustion of coal, oil, gas, biomass, agricultural materials, and waste as well as from industrial and chemical activities^{1–4}. AA have been observed to significantly absorb and scatter incoming solar radiation, resulting in detectable cooling at the surface and simultaneous heating of the atmosphere^{5,6}. This warming may enhance local atmospheric stability and also may lead to decreased cloud cover via the semi-direct effect, both of which effect the local hydrological cycle^{7–11}. It has also been observed over several regions that the net radiative impact of AA on average is larger than CO₂ and other long-lived greenhouse gases in tandem^{12–14}.

The aerosol global radiative forcing mean is estimated to be -0.9 W m^{-2} with an uncertainty range from -1.9 to -0.1 W m^{-2} ¹⁵. Unlike greenhouse gases which always exhibit a positive top of the atmosphere radiative forcing (TOA), the local effect of aerosols on TOA can be either positive or negative^{16,17}, with BC in specific known to exhibit a net positive TOA when located over highly reflective surfaces^{5,18} or at high loadings in general^{19–22}. This is due to the fact that the aerosol direct radiative forcing (DRF) depends upon the total number of particles in the atmospheric column and the particle-by-particle optical properties (i.e., the single scattering albedo (SSA) and asymmetry parameter (ASY)), which in turn depend on the aerosol concentration, mass, size, shape and mixing state^{23–26}. The SSA has a large impact on TOA which has been shown to even be able to switch from positive to negative with a local change of only 11%^{27,28}. This problem is particularly acute since the most reliable current measurements of SSA are from AERONET, which has an uncertainty of 0.03 under moderately and heavily polluted conditions, with the error not well constrained under cleaner conditions^{29,30}.

The scientific community is actively debating and exploring how to accurately simulate the aerosol mixing state and in situ composition^{31,32}. Particle morphology and composition are frequently modeled using external and/or internal mixtures, although observations tend to show that a core-shell mixture is more realistic, although still not sufficiently complex approach^{12,33,34}. This has been observed to be particularly so under more urban and biomass burning impacted areas, which dominate inside of Asia^{12,35,36}. Furthermore, all observations from AERONET assume a core-shell structure of aerosol, and therefore any comparison not including this will be biased³⁷. For these reasons, it has been demonstrated that the aerosol mixing state assumption, is one of the least reliable aspects when computing aerosol optical depth (AOD) and SSA³⁸. AA are short lived on average (1–2 days), but under dry and stable conditions can exist for a week or longer^{39,40}.

The DRF of BC is dependent on the particle size, shape, amount of mixing with scattering secondary aerosols and aerosol precursor vapors, and aerosol aging, as confirmed by laboratory studies^{41,42} in situ observations^{43,44} and models^{45–47}. Current estimates of TOA BC from fossil fuel and biofuel sources vary by a factor of more than two with studies finding a range from 0.08 to 1.27 W m^{-2} ^{22,15}. Excluding a few advanced research models^{48,49}, most climate models have limited ability to incorporate mixing state, aging and particle size information, and therefore do not adequately represent observed particle absorption efficiency^{50,51}. Although the 6th IPCC assessment report estimated BC DRF range from -0.28 to 0.41 W m^{-2} and an associated TOA increase by 0.1 °C on global average⁵², the assessment ignored all high BC emissions products, and furthermore only used emissions products derived from some models (e.g., UKESM1) involved in CMIP6 (used in the IPCC AR6), and therefore, not based upon the current varying atmospheric absorption observations and BC morphology^{53–55}. Therefore, their reported reduction of up to 50% in the warming impacts of BC is as a result of modifying its rapid

¹School of Environment and Spatial Informatics, China University of Mining and Technology, Xuzhou, China. ²Department of Energy, Environmental, and Chemical Engineering, Washington University in St. Louis, St. Louis, MO, USA. ³Carbon Neutrality Institute, China University of Mining and Technology, Xuzhou, China. ✉email: jasonbc@alum.mit.edu

Table 1. Statistical metrics of TOA, ATM and BOA forcing ($W m^{-2}$) over Lumbini and Taihu.

Statistical metrics	AERONET TOA	COSMO TOA	AERONET ATM	COSMO ATM	AERONET BOA	COSMO BOA
Min	−79	−90	5.1	0.1	-1.9×10^2	-2.1×10^2
Max	−10	19	1.5×10^2	2.3×10^2	−27	−18
Mean	−32	−19	34	41	−65	−60
30th	−33	−23	17	21	−75	−71
Median	−29	−18	32	37	−62	−56
70th	−26	−13	44	53	−48	−41
Min	<i>−1.2 × 10²</i>	<i>−1.4 × 10²</i>	<i>5.8</i>	<i>0.1</i>	<i>−2.2 × 10²</i>	<i>−2.6</i>
Max	<i>−20</i>	<i>−5.2</i>	<i>1.2 × 10²</i>	<i>2.0 × 10²</i>	<i>−39</i>	<i>−22</i>
Mean	<i>−57</i>	<i>−42</i>	<i>29</i>	<i>32</i>	<i>−86</i>	<i>−77</i>
30th	<i>−66</i>	<i>−52</i>	<i>18</i>	<i>19</i>	<i>−99</i>	<i>−87</i>
Median	<i>−52</i>	<i>−42</i>	<i>26</i>	<i>28</i>	<i>−79</i>	<i>−71</i>
70th	<i>−44</i>	<i>−33</i>	<i>36</i>	<i>42</i>	<i>−64</i>	<i>−58</i>

Numerical figures for Taihu are represented in bold and italicized format.

climate and cloud based responses, not based on the observed direct and semi-direct heating⁵⁶. Several studies using both top down and bottom up perspectives in tandem^{4,53} have reported that the loadings and radiative forcing of BC are larger than the range estimated by the 6th IPCC Assessment Report, indicating that the overall model range is too narrow. Furthermore, there were no models used in the assessment report that included the consideration of the impacts of mixing state, size and aging, although there are few such models which have made estimations both at regional^{46,57–59} and global level⁶⁰.

Observations of these characteristics are often obtained through photometric satellite sensors with a single viewing angle, leading to a relatively high uncertainty with respect to aerosol absorption⁵³. Furthermore, most models uniformly underestimate measurements of atmospheric absorption that happen in the ultra-violet (UV) and blue wavebands (wavelengths <500 nm), implying that they may have a negative bias and hence underestimate the total effect of BC, BrC, and other sub-micron-sized absorbing aerosols^{61,62}. This finding, if proven, would then indicate that these same models would potentially overestimate the effects of long-lived greenhouse gases warming⁶³. Furthermore, it has been demonstrated that reducing these uncertainties is significant when calculating aerosol number concentrations—a key variable in accurately estimating aerosol-radiation and aerosol-cloud interactions^{64,65}. Thus, due to a lack of dependable global distribution data, quantitative estimations of atmospheric aerosol absorption forcing are prone to considerable uncertainty.

This work uses observations from AERONET in combination with a MIE-model-inversion approach to constrain the probability distribution in terms of size, number, and mixing state of BC (cores) surrounded by scattering aerosol (i.e., sulfate and nitrate) shells, from observations at multiple wavelengths. Next, this work applies the radiative transfer model and computes the DRF at the TOA and in the atmosphere itself (ATM), in a joint process herein referred to as COSMO. The variation and uncertainty in TOA and ATM are analyzed with respect to particle size and mixing state, and the non-linear nature of this interaction is quantified and explained. Since this approach computes a probabilistic distribution, the findings mark an important step forward, and when combined with future remote sensing and in situ microphysical and size-based observations, will yield further and deeper findings. The study also produces a set of linear corrections which can be applied rapidly to forcing calculations within the context of global models, allowing for the current generation of Global climate models (GCMs) to rapidly include these effects, until more

robust techniques backed by more and higher quality observations can be employed.

RESULTS

Overview of radiative forcing and AOD

Table 1 and Fig. 1 demonstrate the general statistics and probability density functions (PDF) for TOA and ATM using COSMO and AERONET at Lumbini and Taihu respectively. The PDFs of COSMO-ATM cover a wider range of values than AERONET-ATM, with the mean, 30%, median, and 70% probability values of COSMO-ATM all larger than AERONET-ATM, indicating that the greater atmospheric heating is consistent across the distribution. In the case of surface (BOA) forcing, COSMO-BOA shows both a larger spread and a less negative value than AERONET-BOA, indicating a net reduction in surface cooling. Unlike ATM, there are more significant differences in BOA where at Taihu the spread is wider, although the statistics at the 30%, 50%, and 70% level are similar.

Due to these results, the differences between COSMO-TOA and AERONET-TOA have a wider spread at Lumbini, and in both locations COSMO-TOA exhibits a significantly large amount of its upper statistical range of solutions towards less negative forcing values (less cooling). Overall, 17.9% and 3.3% of solutions are respectively above the maximum of AERONET-TOA at Lumbini and Taihu. Furthermore, 1.9% of the COSMO-TOA values at Lumbini produce a net positive TOA (net aerosol climatological heating).

The observed larger spread in ATM and a simultaneous less cooling TOA is consistent with the joint effects of changes in BC aging and BC size on the per-particle optical properties, with modeling studies done by Wu et al.⁶⁶ demonstrating that BC could obtain a positive regional TOA after significant aging, Cohen et al.¹² demonstrating a global increase in TOA as a function of the change in the size of aged BC, and Ramana et al.⁶⁷ showing that a critical ratio of BC to sulfate can yield a positive TOA. Supplementary Fig. 1 shows the PDF of surface spectral albedo, BC sizes, and size ratio solutions at the two sites, indicating that the two sites have significant differences in these aspects. Lumbini has a higher surface albedo and both a larger median and maximum core BC size than Taihu, while Taihu has particles with larger shell to core ratio than Lumbini, implying that on average, BC is emitted with larger sized cores at Lumbini as compared to Taihu, while overall the particles observed in Taihu are more aged and coated, over all BC core sizes, than those at Lumbini. It based on these observed differences that the diversity of solutions of

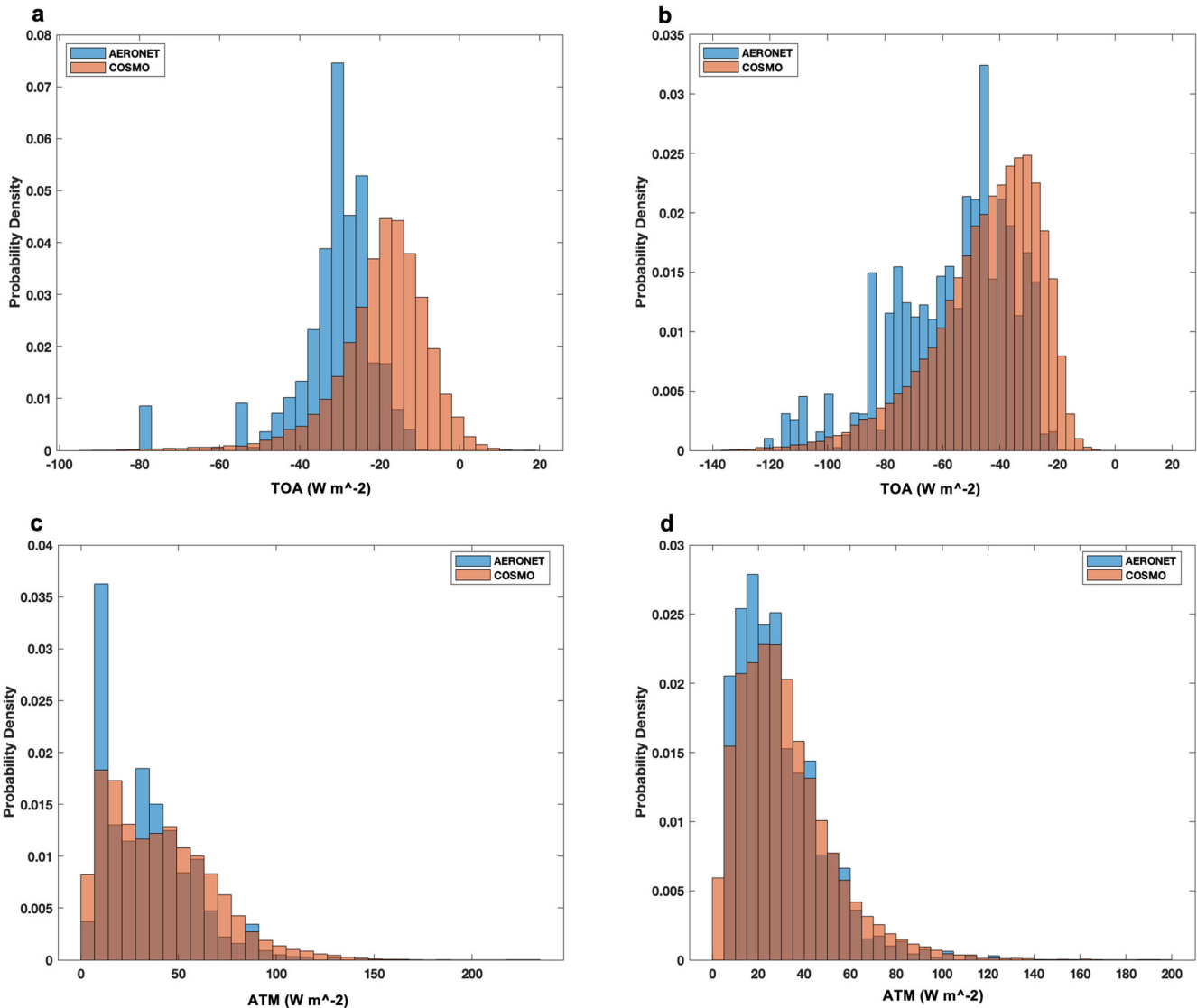


Fig. 1 Probability density distributions of top-of-atmosphere (TOA) and atmospheric (ATM) radiative forcing. Distributions were derived from AERONET and COSMO data for the Lumbini (a, c) and Taihu (b, d).

radiative forcing occur at both sites and between the sites and AERONET, which itself assumes a fixed size distribution and constant aerosol core to shell ratios across sizes.

Radiative forcing under different AOD conditions

The distributions of TOA and ATM under different AOD conditions were analyzed and statistical metrics presented, with the COSMO-TOA mean, median, 30% and 70% value all less negative (less cooling) than the AERONET-TOA across all AOD conditions at both Lumbini and *Taihu* (the values underlined are for Lumbini while *italics* are for *Taihu*). Under clean AOD conditions the mean [AERONET-TOA/COSMO-TOA] was $[-25, -36/-17, -29]$ W m^{-2} , while under polluted AOD conditions the mean shifted more negative (more cooling) and simultaneously broadened their distribution with the mean values $[-43, -80/-36, -65]$ W m^{-2} respectively. Across all values and percentiles, as the AOD increases, both sites shift to a more negative TOA, with the shift in Lumbini always smaller than in *Taihu*, while the shift in the breadth in Lumbini is always larger than in *Taihu*.

Extending this analysis across the entire range of results (Supplementary Fig. 2), the relationship between TOA and AOD

at both sites are fairly linear, with a less negative slope in both Lumbini (-22.9 versus -12.8 , $p < 0.05$) and *Taihu* (-36.2 versus -28.2 , $p < 0.05$) in the case of COSMO-TOA. In addition to less cooling per unit change of AOD, the breadth of possible solutions, particularly on the less cooling and/or warming side increases as the AOD increases. The overall difference between AERONET-TOA and COSMO-TOA is positive (COSMO-TOA is less negative) and ranges $[13 \pm 8.1/16 \pm 12]$ W m^{-2} respectively.

When the TOA is grouped by probabilistic percentiles from 10th to 90th (Supplementary Table 1) the distribution is observed to gradually become more negative at all percentiles. This rate of decrease for AERONET-TOA is always more negative than for COSMO-TOA, in particular under polluted and extremely polluted conditions in Lumbini and under moderately polluted, polluted, and extremely polluted conditions in *Taihu*. In Lumbini, the least negative relationship is in clean conditions from the 10th to 40th percentile and next in fairly polluted conditions from the 40th to 90th percentile, while in *Taihu* the least negative relationship is always in clean conditions. Interestingly, at the top 5% of the probability distribution, Lumbini has some positive TOA values (net aerosol heating) across all AOD conditions, with a maximum

Table 2. Mean (median) of TOA and ATM forcing ($W m^{-2}$) across different AOD and BC size conditions over Lumbini and Taihu.

AERONET TOA	COSMO TOA	AERONET ATM	COSMO ATM	BC core size	Pollution condition	AERONET TOA	COSMO TOA	AERONET ATM	COSMO ATM
-27 (-29)	-23 (-22)	13 (11)	13 (12)	Small	Clean	-36 (-35)	-34 (-32)	16 (14)	16 (15)
-29 (-30)	-25 (-23)	15 (12)	19 (18)	Small	Fairly polluted	-47 (-45)	-43 (-41)	21 (23)	21 (20)
-34 (-34)	-27 (-25)	19 (17)	26 (23)	Small	Moderately polluted	-64 (-62)	-58 (-55)	22 (18)	26 (25)
-52 (-49)	-40 (-38)	31 (23)	41 (42)	Small	Polluted	-81 (-76)	-75 (-72)	37 (34)	38 (35)
-26 (-29)	-17 (-17)	17 (14)	18 (12)	Medium	Clean	-36 (-35)	-31 (-30)	19 (18)	22 (22)
-28 (-29)	-19 (-18)	22 (17)	28 (20)	Medium	Fairly polluted	-47 (-45)	-41 (-40)	25 (25)	30 (30)
-32 (-32)	-21 (-20)	34 (35)	47 (50)	Medium	Moderately polluted	-64 (-62)	-52 (-51)	27 (19)	37 (31)
-42 (-39)	-27 (-26)	54 (54)	67 (68)	Medium	Polluted	-80 (-76)	-65 (-63)	43 (38)	43 (33)
-24 (-25)	-14 (-14)	25 (21)	26 (19)	Moderately big	Clean	-37 (-37)	-29 (-29)	23 (23)	27 (22)
-27 (-27)	-14 (-15)	31 (31)	37 (31)	Moderately big	Fairly polluted	-47 (-46)	-37 (-36)	27 (26)	31 (26)
-31 (-31)	-16 (-16)	45 (48)	57 (57)	Moderately big	Moderately polluted	-64 (-63)	-46 (-45)	30 (23)	38 (30)
-39 (-36)	-20 (-20)	54 (52)	71 (69)	Moderately big	Polluted	-81 (-77)	-55 (-53)	45 (41)	39 (33)
-20 (-20)	-7.0 (-7.2)	37 (38)	37 (33)	Big	Clean	-36 (-37)	-23 (-22)	27 (26)	29 (27)
-25 (-27)	-7.8 (-8.2)	40 (35)	44 (40)	Big	Fairly polluted	-46 (-46)	-28 (-28)	34 (33)	35 (32)
-29 (-28)	-8.1 (-8.2)	52 (53)	61 (59)	Big	Moderately polluted	-63 (-62)	-36 (-35)	38 (42)	45 (44)
-35 (-34)	-12 (-13)	60(59)	62 (55)	Big	Polluted	-78 (-77)	-43 (-42)	60 (58)	52 (45)
-18 (-19)	-3.2 (-4)	41 (42)	39 (40)	Extremely big	Clean	-33 (-31)	-18 (-18)	32 (29)	35 (33)
-23 (-22)	-3.3 (-3.6)	48 (46)	51 (51)	Extremely big	Fairly polluted	-43 (-42)	-23 (-23)	43 (48)	40 (40)
-26 (-28)	-3.6 (-2.6)	62 (66)	67 (68)	Extremely big	Moderately polluted	-57 (-58)	-28 (-29)	56 (50)	61 (64)
-32 (-34)	-5.9 (-7.2)	72 (59)	82 (65)	Extremely big	Polluted	-59 (-58)	-33 (-33)	82 (84)	81 (78)

Numerical figures for Taihu are represented in bold and italicized format.

number of cases (0.7%) with net positive COSMO-TOA under moderately polluted conditions observed which reduced to a least number of cases (0.2%), under polluted conditions. Although there are no positive values in TAIHU-TOA, at the top 5% of the probability distribution Taihu has a maximum of 2.9% of solutions larger than the maximum of AERONET-TOA that fall under clean AOD conditions, which reduces to only 0.3% values under polluted conditions.

Based on Xu et al.⁶⁸ and Liu et al.⁶⁹ ATM forcing should linearly increase (more warming) in a smooth manner as a function of AOD. However, the results herein show a different conclusion, with the mean/median AERONET-ATM; COSMO-ATM under clean conditions [21/14,21/20; 21/17,23/21] $W m^{-2}$ and [48/47,42/37; 60/58,41/35] $W m^{-2}$ under polluted conditions, clearing demonstrating that the change is not uniform. The increase in warming is faster and the range is broader in the case of COSMO-ATM compared with AERONET-ATM, even though the change in AOD is the same. Furthermore, even though COSMO-ATM has a positive mean which is larger than AERONET-ATM, certain values are smaller than the minimum of AERONET-ATM.

Radiative forcing under simultaneous changes in BC size and AOD

In Lumbini the core/shell assumption herein has been shown to match well with observed environmental conditions, where BC dominates the aerosol extinction⁷⁰, although previous work has not been able to quantify the size of the BC cores, which this work shows are dominated (55.1%) by small and medium core sizes (≤ 120 nm), while only 4.1% is extremely big core sizes (>200 nm). The results show there is a statistically significant temporal

variation across all percentiles, where data from November and December always has larger core sizes, and data from February and September always has smaller core sizes, while the largest core sizes are found in March at the 75th percentile and above. This temporal and size-based analysis matches well with the temporal and source variation previously observed in Lumbini, including impact of both transported and local sources and seasonal variation, while further more precisely quantifying the core sizes at a month-to-month resolution, allowing for a more precise match with the known changes in the arrival of the Monsoon and biomass burning timing⁷¹⁻⁷³.

In Taihu, the BC size distribution shows that 54.5% of cores are small and medium in size ($BC \leq 100$ nm), while 3.1% of cores are extremely big (>170 nm). These sizes are consistent with the long-term observation site of BC core size in the general urban background in Chinese megacity Beijing, which is similar in terms of GDP per person and energy consumption with Taihu and its surrounding area⁷⁴. There is a very short campaign in an urban street canyon in neighboring Nanjing, in which the BC core size can also be reproduced under heavily polluted conditions⁷⁵. The results show a statistically significant temporal variation where data from March, November, and December always have larger core sizes across all percentiles, while in July the largest core sizes are found, but only at the 95th percentile. These timings again agree well with the timing of both the Monsoon dry phase and when biomass burning occurs^{76,77}.

Statistical metrics of TOA and ATM under different BC core sizes and AOD conditions are presented in Table 2 and visualized for small and extremely big core sizes under clean and polluted conditions in Fig. 2.

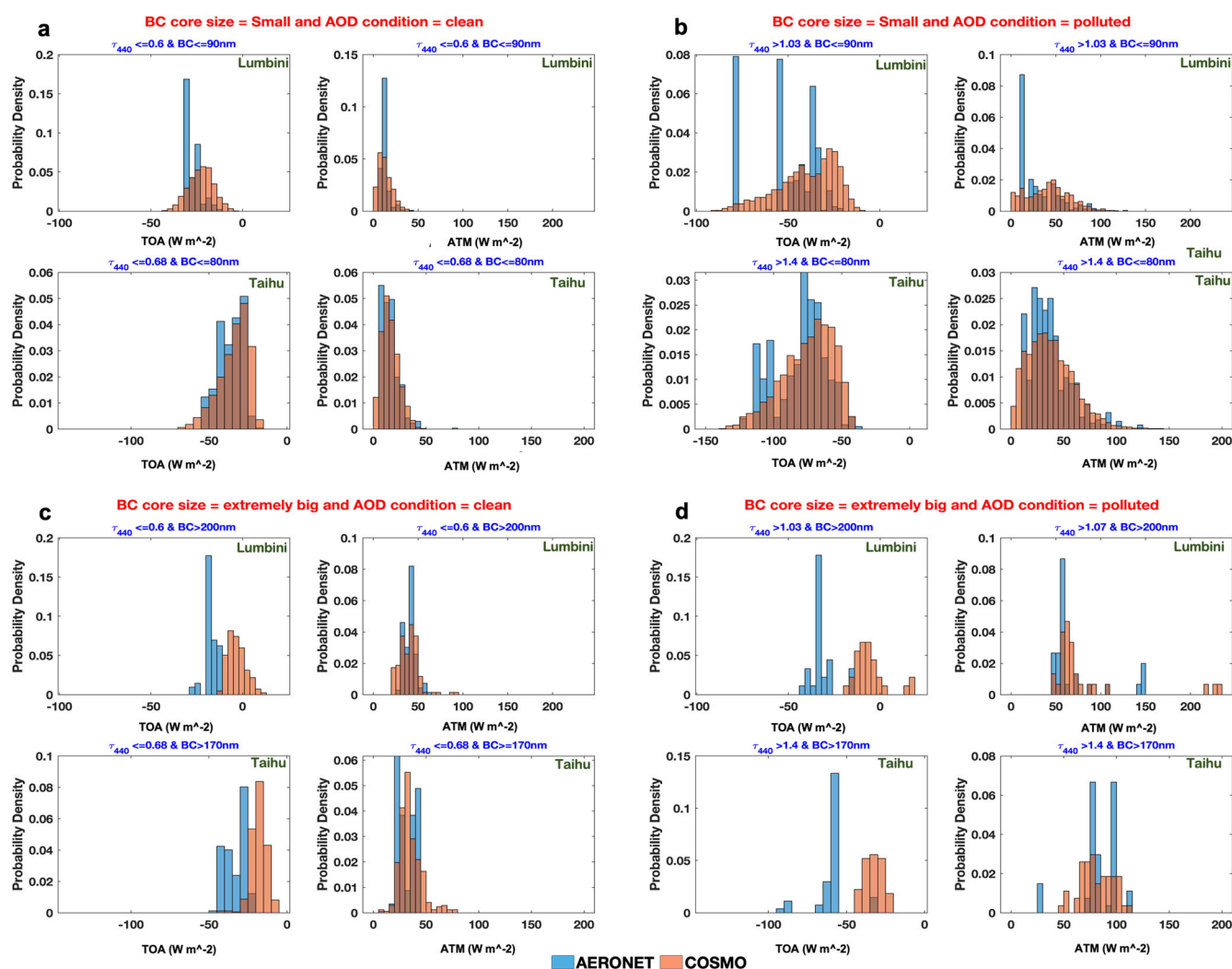


Fig. 2 Probability density distributions of top-of-atmosphere (TOA) and atmospheric (ATM) radiative forcing from AERONET and COSMO data. Distributions are shown for varying black carbon (BC) core sizes under different aerosol optical depth (AOD) conditions. The upper panels display distributions for small BC core sizes under clean (a) and polluted (b) AOD conditions. The lower panels show distributions for extremely large BC core sizes under clean (c) and polluted (d) AOD conditions.

First, irrespective of the core size, AOD condition, or site, COSMO-TOA always has a less negative value than AERONET-TOA, including both when varying core size at constant AOD, as well as when varying AOD at constant core size. COSMO-TOA becomes negative more slowly for each and every fixed AOD condition as the BC size increases (aerosols are less cooling) at both Lumbini and Taihu, similar to findings by^{67,78}. However, the rate of change is slower at Lumbini across all AOD conditions as the core size increases than in Taihu. Specifically, in Lumbini the rate of change varied from a maximum of 0.8 W m^{-2} under moderately clean and fairly polluted AOD to a minimum of 0.5 W m^{-2} for polluted AOD conditions, while in Taihu, the rate of change in TOA varied from a maximum of 3.4 W m^{-2} under moderately clean conditions to a minimum of 1.0 W m^{-2} under polluted conditions. Oppositely, the rate of change for each fixed BC size with changing AOD conditions demonstrates a larger rate of change in Lumbini with a maximum of 23 W m^{-2} for extremely big cores to a minimum of 3.8 W m^{-2} for medium sized cores, than at Taihu, where the change 0.9 W m^{-2} was smallest for extremely big cores, and was largest, 1.9 W m^{-2} for small BC cores. This non-linearity demonstrates that locally defined core size categories and AOD pollution

levels are highly non-uniform and non-transferable in terms of particle-by-particle optical properties.

Secondly, COSMO-TOA under different size and AOD conditions show a multimodal distribution at both Lumbini and Taihu. In Lumbini under small BC core and clean AOD conditions, the TOA was distributed normally, evolving into a mixture of two normal equations (skewed towards less negative TOA values) as the AOD conditions increased to polluted. In case of Taihu under small core conditions regardless of AOD, the solution of the distribution of TOA was always fitted by a mixture of two normal equations (skewed towards less negative TOA values). These results suggest a more complex distribution of forcing than a single lognormal or set of static bins (Supplementary Fig. 3) can readily account for. This is indicative that precision in terms of both the BC core size and AOD conditions is required to successfully analyze the TOA. For these reasons, a simple linear scaling between TOA and AOD will always yield a net TOA which is too negative, which in turn could account for bias in climate models that are adapting such a scaling approach.

Next, over Lumbini, the mean and median values of COSMO-ATM were always greater than those of AERONET-ATM, with the exception of clean AOD conditions for big and extremely big BC

core sizes. At Taihu, the COSMO-ATM mean and median were greater in all cases except when BC size cores were medium to extremely big and when BC size cores were small and/or extremely big under fairly polluted AOD conditions. When analyzing the change in ATM for each fixed BC size pursuant to increasing AOD conditions, it is observed that ATM forcing becomes stronger for all BC sizes as AOD increases. When AOD was fixed and the BC core size increment was analyzed for both COSMO and AERONET ATM, parallel increases were observed. Both sites exhibited a non-uniform rate of change in ATM, similar to TOA. The rate of change in ATM, when analyzed with varying AOD conditions at each fixed BC core size, revealed that at Lumbini, for small BC core sizes, the ATM changed by 2.8 W m^{-2} when the AOD changed from clean to polluted, whereas for big BC cores, the rate of change was slower and was observed to be 0.2 W m^{-2} . When solutions for Taihu were analyzed under the same conditions, it was discovered that extremely big BC cores exhibited the fastest rate of change in ATM by 4.3 W m^{-2} , while medium BC cores exhibited the slowest rate of change 0.3 W m^{-2} . Similarly, the rate of change in ATM was non-uniform and irregular when analyzed for changing BC core sizes under fixed AOD conditions, whereas at Lumbini, the rate of change in ATM forcing from small to extremely large BC core size was slow and less than 1 W m^{-2} with changing size at each AOD. In the case of Taihu, the rate of change was observed to be as high as 6 W m^{-2} for highly polluted AOD conditions and as low as 0.6 W m^{-2} for fairly polluted conditions, corresponding to the change in BC core sizes.

It is to be noted that these non-linearities highlighted pertain to submicron sizes aerosols. Which in turn generally show a large change in and extinction coefficient in terms of core size, as well as a large number difference in terms of changes in mass, since the total extinction is a function of the number times the extinction per particle. Clearly, the current assumption of a fixed and simple size distribution consisting of a bimodal lognormal distribution of one fine-mode and one coarse-mode size do not account for the variations observed and explained above, in which specific non-linearity within fine mode fraction adds to the uncertainty in DRF estimates.

Radiative forcing under simultaneous changes in aging and AOD

Additionally, this non-linearity can be further be explained by changes in the scattering and/or absorption individually on a particle-by-particle basis, not merely the extinction. This is especially so at high aerosol number, where multiple scattering will play a larger role in the total column radiative forcings computed. For this reason, a deeper look needs to also consider any coating that exists on the aerosol particles, since as BC ages, the particles become more densely coated, and thereby change both absorption due to lensing, as well as scattering due to multiple internal refractions^{79,80}.

Statistical metrics including the mean and median of both TOA and ATM under different mixing state and AOD conditions are tabulated in Table 3. First, irregardless of the mixing state and AOD conditions, COSMO-TOA is always less negative than AERONET TOA for Lumbini. This hold true for both when the AOD is held constant and the mixing ratio increases, as well as when the mixing ratio is held constant and the AOD increases. While for Taihu, the COSMO-TOA is always less negative in all cases except when the AOD conditions are polluted and AA are extremely heavily coated, when COSMO-TOA is more negative. Furthermore, these more negative changes in TOA are not at all uniform within the individual sites and rate of change is larger in case of Lumbini than in Taihu, when TOA change at each fixed coating stage was analyzed for AOD change from clean to polluted. For both the sites, the rate of change to more negative was high in case of heavily and extremely heavily coated BC cores

with increasing AOD conditions. Second, COSMO-ATM is only greater than AERONET-ATM at Lumbini under barely coated through substantially conditions, as well as heavily coated conditions where the AOD is fairly polluted or more, and less under other conditions. At Taihu, COSMO-ATM is only greater than AERONET-ATM under barely coated conditions, moderately coated conditions which are not polluted, and substantially coated conditions which are either clean or moderately polluted. At both sites, under highly coated conditions and clean to moderately polluted AOD there is always a switch in the direction of the ATM forcing from increasing to decreasing and back to increasing again, as the AOD increases. All of the areas in which the switch in sign occur happen when the ATM forcing is relatively low (under 10 W m^{-2}) indicating that the particles overall are not contributing a sufficient amount of forcing to induce vertical or other atmospheric dynamical changes, and therefore this effect is purely local and radiative in nature.

In Lumbini, the barely coated to heavily coated BC cores showed an increasing mean COSMO-ATM forcing with increasing AOD, which grows fastest for barely coated particles, grows moderately fast for moderately and substantially coated particles, and grows slowest for heavily coated particles. In Taihu this is slightly different, where the fastest increase occurs for both barely coated and moderately coated, while a moderate increase occurs for substantially coated. At both stations, the ATM forcing decreases at constant AOD condition as the coating increases. While, this decrease in ATM at constant AOD gets larger as the magnitude of the AOD increases.

To better analyze the weakening ATM across mixing states, the ATM across both mixing state and BC core size is analyzed in tandem. At Lumbini small (at the 90th percentile) and medium (at the 30th percentile and above) BC cores have an increase in ATM forcing as the coating increases, but then subsequently changes direction and drops from moderately coated upwards. In Taihu this is observed only at small BC core sizes at the 50th percentile and above. However, when examining moderately big and larger BC cores, the ATM forcing always becomes less positive as the coating increases. This suggest that the per-particle lensing effect of absorption enhancement increases the net absorption when the BC sizes are relatively small ($\leq 120 \text{ nm}$) (Supplementary Table 2). Beyond this size range, the efficiency of the BC absorption enhancement decreases, although it is still a net positive effect under all conditions.

Next, the distribution and variation in ATM and TOA forcing for barely mixed (ratio ≤ 25 th percentile) and heavily coated (ratio > 75 th percentile) under clean and polluted conditions were investigated as shown in Fig. 3. For AERONET, the difference in TOA and ATM forcing across different mixing states is generally a constant value along any given line with a constant slope. The value does vary from one slope to another, but not along that path. However, this is not the case with the COSMO-TOA and COSMO-ATM forcings. The function is both non-linear along a given slope as well as at different slope angles. This change in forcing is quite significant, at times up to 50% of the initial value, and frequently both increasing and decreasing along different parts of the sloped path. These changes correspond to changes occurring at the same mixing ratio, but at different core sizes of BC as well as under different values of AOD. This clearly shows how both the size and mixing state play an important role in determining the median value as well as its variation, for both TOA and ATM forcing. In the case of COSMO, these changes in both TOA and ATM happen everywhere in terms of BC core along each sloped mixing ratio path, following a wavelike pattern, with a distance between the crests and peaks occurring irregularly but over a size change in BC core ranging from 30 to 80 nm.

Table 3. Mean (median) of TOA and ATM forcing $W m^{-2}$ across different AOD and coating conditions over Lumbini and Taihu.

AERONET TOA	COSMO TOA	AERONET ATM	COSMO ATM	Coating condition	Pollution condition	AERONET TOA	COSMO TOA	AERONET ATM	COSMO ATM
-18 (-19)	-7.2 (-7.6)	41 (41)	45 (44)	Barely coated	Clean	-34 (-33)	-26 (-25)	30 (29)	34 (32)
-22 (-21)	-8.6 (-9.1)	48 (46)	56 (54)	Barely coated	Fairly polluted	-44 (-45)	-33 (-32)	37 (38)	45 (42)
-26 (-27)	-10 (-11)	59 (59)	71 (68)	Barely coated	Moderately polluted	-60 (-60)	-41 (-40)	44 (46)	60 (57)
-34 (-34)	-16 (-17)	77 (74)	88 (83)	Barely coated	Polluted	-70 (-71)	-51 (-49)	71 (70)	82 (79)
-21 (-23)	-13 (-12)	28 (30)	29 (27)	Moderately coated	Clean	-37 (-37)	-30 (-29)	20 (19)	22 (21)
-27 (-27)	-14 (-14)	32 (32)	39 (38)	Moderately coated	Fairly polluted	-48 (-46)	-39 (-37)	27 (26)	30 (29)
-31 (-31)	-15 (-15)	42 (38)	53 (52)	Moderately coated	Moderately polluted	-63 (-62)	-47 (-46)	34 (35)	42 (41)
-38 (-36)	-22 (-22)	61 (59)	68 (64)	Moderately coated	Polluted	-82 (-77)	-58 (-56)	56 (57)	53 (48)
-26 (-25)	-18 (-17)	16 (14)	18 (17)	Substantially coated	Clean	-37 (-38)	-32 (-30)	14 (14)	15 (14)
-30 (-31)	-20 (-19)	21 (22)	26 (24)	Substantially coated	Fairly polluted	-49 (-48)	-40 (-39)	20 (23)	20 (19)
-35 (-34)	-23 (-22)	27 (32)	36 (36)	Substantially coated	Moderately polluted	-64 (-66)	-52 (-50)	22 (18)	29 (28)
-43 (-40)	-28 (-27)	30 (28)	50 (47)	Substantially coated	Polluted	-83 (-79)	-65 (-63)	40 (38)	39 (36)
-28 (-29)	-22 (-21)	12 (11)	8.7 (8.3)	Heavily coated	Clean	-39 (-40)	-34 (-32)	11 (10)	8.2 (7.6)
-28 (-30)	-23 (-21)	11 (10)	13 (13)	Heavily coated	Fairly polluted	-46 (-45)	-41 (-38)	13 (11)	9.3 (9.3)
-36 (-34)	-27 (-26)	10 (5.1)	14 (14)	Heavily coated	Moderately polluted	-68 (-66)	-56 (-53)	17 (17)	14 (13)
-64 (-56)	-47 (-45)	14 (14)	24 (25)	Heavily coated	Polluted	-80 (-75)	-73 (-70)	27 (26)	21 (20)
-30 (-29)	-26 (-24)	11 (11)	4.3 (4.1)	Extremely heavily coated	Clean	-41 (-41)	-37 (-35)	8.4 (9.4)	4.4 (4.0)
-28 (-30)	-27 (-23)	8.4 (7.1)	5.8 (5.4)	Extremely heavily coated	Fairly polluted	-44 (-45)	-40 (-37)	7.8 (6.8)	3.2 (3.0)
-34 (-34)	-30 (-27)	5.1 (5.1)	5.2 (5.3)	Extremely heavily coated	Moderately polluted	-70 (-71)	-58 (-54)	16 (16)	6.1 (5.4)
-67 (-67)	-54 (-50)	12 (12)	10 (10)	Extremely heavily coated	Polluted	-79 (-79)	-81 (-79)	22 (20)	10 (9.5)

Numerical figures for Taihu are represented in bold and italicized format.

Adjusting the TOA: a small step to tackle the complex relationship

Since quantifying TOA is a time consuming and challenging task for models, many have approximated this using a directly linear function of the AOD, even though this work has demonstrated that this is not sufficient to capture the high amounts of non-linearly in the TOA response. To improve this approach and allow the current generation of global climate models to rapidly reduce their TOA uncertainty with respect to submicron aerosols as observed herein, an improved multi-regression linear model inclusive of BC core size and mixing ratio is proposed.

Predicted TOA values were computed for two linear models, one containing only TOA and AOD, and another containing TOA, AOD, BC (size), and ratio. Goodness of fit was then made based on the retrieved AERONET-TOA, showing that including BC size and mixing state information improves all three statistics over both sites, where the R-squared statistic ($p < 0.05$) increased, while the RMSE and MGE statistics both decreased (details in Fig. 4 and

Supplementary Table 3). In all cases, the AOD is still the single largest driver, but the mixing ratio is of similar order of magnitude, while the BC size is an order of magnitude smaller, but still not insignificant. It is hoped that a further improved product can be made, to continue improving the results herein.

DISCUSSION

Recent studies still continue to demonstrate that the uncertainty in the aerosol radiative forcing is one of the largest components of the total climate uncertainty. They also demonstrate that the Earth is warming faster than model estimates based on the current generation of GHG emissions and precursors. Such approaches tend to be quite simple and assume at most a single mode of aerosols in the fine mode, leading to an underestimate of the overall warming that mixed aerosols and absorbing aerosols actually have on the radiative system. Hence, the results found herein, which indicate that TOA may be less negative and/or the ATM may be both positive, contribute to helping to close the gap

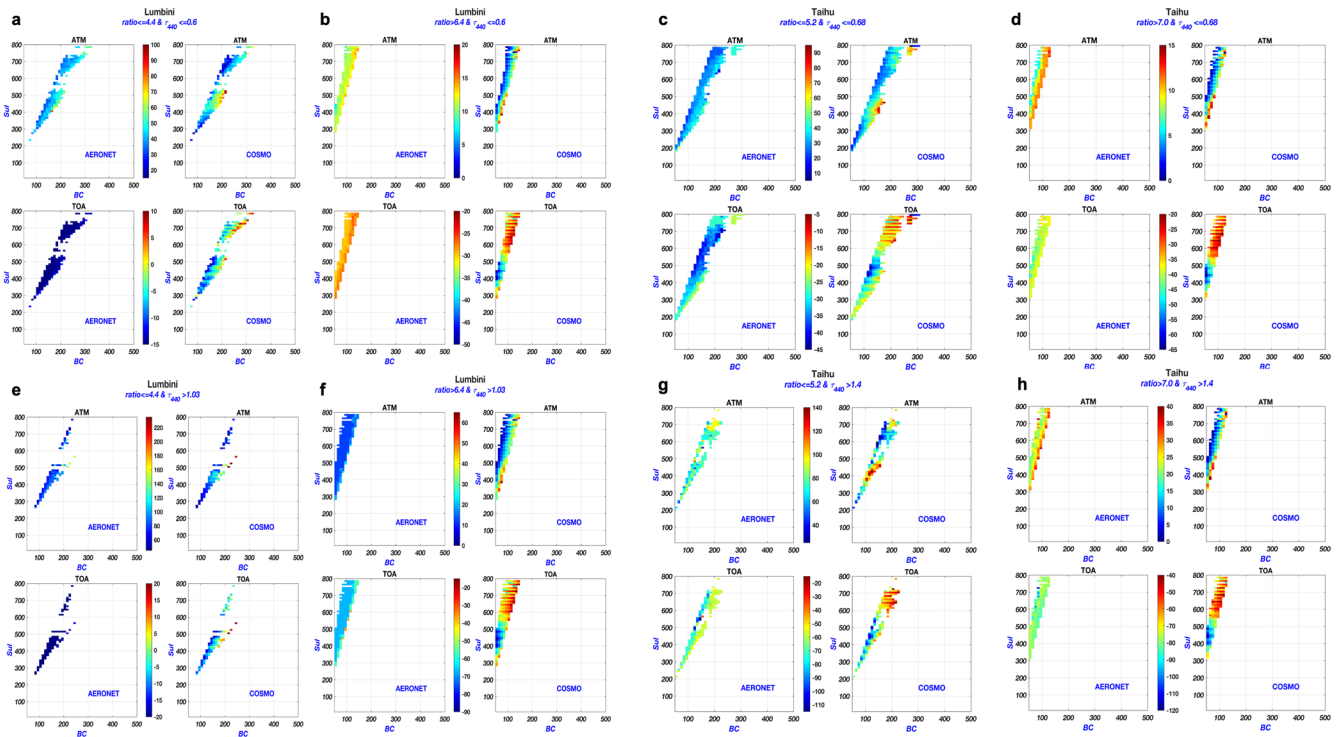


Fig. 3 Distributions of top-of-atmosphere (TOA) and atmospheric (ATM) radiative forcing for Lumbini and Taihu from AERONET and COSMO data. Distributions are shown across varying black carbon (core) and sulfate (shell) particle sizes for different coating conditions and aerosol optical depth (AOD). The upper panel shows ATM and TOA distributions for barely coated particles (**a, c**) and heavily coated particles (**b, d**) under clean AOD conditions. The lower panel shows distributions for barely coated particles (**e, g**) and heavily coated particles (**f, h**) under polluted AOD conditions. The colorbar represents forcing values in W m^{-2} .

on this important scientific conflict in understanding the climate forcing balance that is presently observed and not fully rectified.

This paper helps explain that DRF is influenced by more than just the total aerosol mass loading or average vertically integrated extinction concentration, and also requires a deeper understanding of the size, shape, and mixing state. This is particularly important to consider not only at one wave band, as is traditionally done around the middle of the incoming spectrum at some single value from 500 to 550 nm, but instead across the incoming spectrum including in the ultraviolet, visible and near infrared wavebands, since real aerosol particles absorb and extinct radiation across these bands differently as a function of their physical and optical properties. Furthermore, the fact that current models underestimate the amount of AA compared with remotely sensed measurements, means that using results obtained from observations should yield a reduction in the overall bias, in addition to the uncertainty. This is furthermore exacerbated by the issue that aged aerosols tend to be not well treated by models, and are found to lead to some of the most non-linear forcing changes observed herein.

In this paper, the probabilistic range of all possible solutions of aerosol size, mass, mixing state, and resulting DRF and TOA are computed, based on fulfilling all of the independent optical observations across a wide range of wavelengths. The observations are taken from two different AERONET stations in very different locations within Asia, so as to better represent the variability of regions which have different economic and atmospheric conditions, while also being representative of the fact that much of the Global South is still on average more polluted. This work's range of viable solutions explicitly improves upon the current oversimplification that modeled aerosols use for SSA, scattering, and external/internal mixing, and quantifies a correction that can be applied by present day models to more precisely

compute the associated bias in TOA and/or ATM, under both moderately and heavily polluted conditions. There are additional advantages provided and challenges outlined, since this approach requires knowledge of aerosols from a number-based perspective, not the more traditional mass-based approaches commonly used.

It has commonly been assumed that the theoretical scaling between ATM and AOD applied equally to TOA and AOD. However, the findings from this study, demonstrate two things: first, that while TOA does become more negative as AOD increases, a significant portion of this is governed by particle size and mixing state. Second, this average negative relationship does not hold true across the entire range of solutions, with a small subset of solutions on a per-particle basis producing positive solutions. A better understanding of this subset of conditions, and observations to support quantifying how common it is in the atmosphere can both provide a meaningful boost in mitigation of less cooling TOA and more warming ATM types of conditions. This further suggests that the climate modeling community cannot simply apply this negative relationship as a valid assumption under all cases. It demonstrates that additional work that can be applied to better constrain the particle size and mixing state through observation will lead to an improved ability to bias correct the overall TOA and ATM values. This is most important to consider in the small groups of solutions (up to 1.9% in Lumbini and 3.3% in Taihu) that may lead to either a total sign change of aerosols from negative to positive, or that may change the sign of the trend from a negative association with an increasing AOD to a not-statistically significant association with increasing AOD, or even an increase in AOD leading to warming. The impact of an improved understanding of the particle size and mixing can make a significant impact on the overall understanding of aerosols on radiative forcing, since current aerosol emissions and absorption models generally are based on mass-based absorption

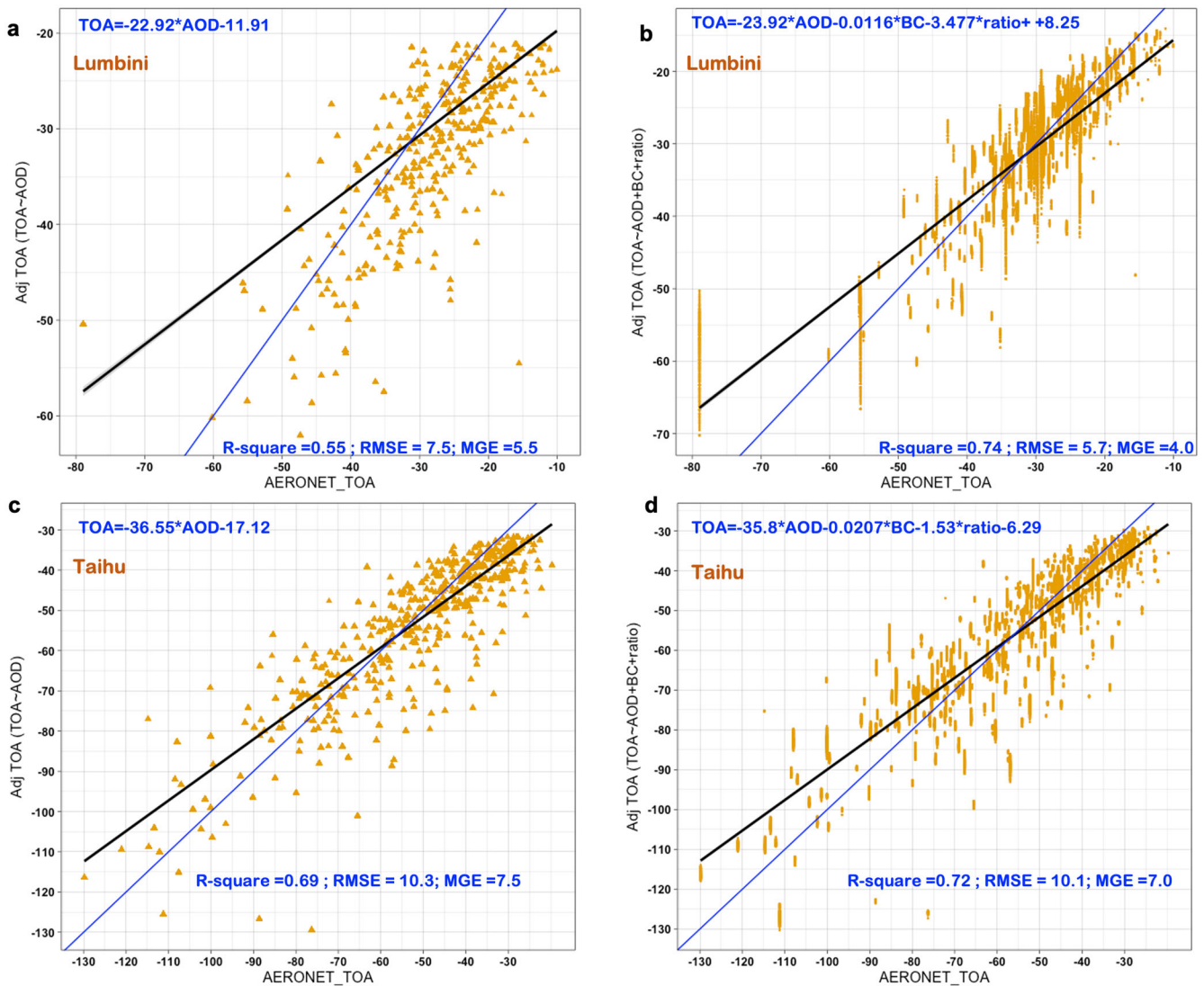


Fig. 4 Deriving adjusted TOA using two different linear models including the effects of BC size and mixing state as additional variables. Two linear models $TOA \sim AOD$ (a, c) and $TOA \sim AOD + BC + \text{ratio}$ (b, d) and their errors and R -square metrics derived for Lumbini and Taihu. Inclusion of black carbon core size and mixing ratio in the multi-regression linear model improves all model statistics—higher R -squared, lower RMSE and MGE—across both sites.

coefficients^{81–83}, which focus mostly on the smaller number of larger sized particles, and favor single size distributions. Given that the community tends to use mass-based observations and absorption coefficients, and that $PM_{2.5}$ and other such observations are more heavily weighted towards a smaller number of very large particles, that active consideration of the size may not be compatible with the current generation of observations, and may require a significant set of new standards to be established.

This result shows that the more complex range of possible sizes and mixing states leads to a growth rate between TOA and ATM which is larger and more variable in the results herein as compared to the single size distribution approach used by AERONET. This shows that the space of possible solutions should account for a multimodal fine mode distribution, as found at both Lumbini and Taihu, which will require far more size-resolved and mixing-resolved observations. Such approaches as adapted by^{37,84–86} assume that there is no larger second or multiple set of models in the submicron aerosols, therein limiting the non-linear feedback and contribute to a lower error, but more biased case in which the lesser cooling TOA and more warming ATM

cases observed herein are no longer possible to model. Given that in situ observations show that there are a significant number of particles in this range that exist in the real world^{87,88}, this adds further importance to quantifying and accounting for this bias.

While the current generation of AERONET forcing inversions show that in case of changing mixing state at different AOD conditions, any line with a constant slope will typically have a consistent value for SSA and therefore little difference between TOA and ATM forcing across different mixing states. Any such mixture with an assumed constant mixing ratio between the BC core and sulfate shell will produce a similar set of TOA and ATM forcings. The results herein instead demonstrate that this is not the case. The response across the mixing ratio between the BC core and sulfate shell varies non-linearly at a constant slope as a function of both the BC core size and AOD. There is also a variation between different sulfate shell sizes with the same slope ratio, with these changes sometimes varying by up to 50% of the average value. These changes are quantified herein, and a correction algorithm is presented to account for this as a function of the BC core size, mixing state, and AOD, in a probabilistic manner.

The results herein demonstrate how improving the quantification of both TOA and ATM forcing requires a greater understanding of both the total size and mixing state of absorbing aerosols, and demonstrates that a failure to account for this has an impact not only on the uncertainty (variation), but also on the mean/median (bias). This work has also provided a detailed and rapid fix for this issue, that should at least help global scale models take this first order association into immediate account. The fix established herein is consistent with the fact that the current surface temperature is rising faster than the modeling community can predict^{89–91}. The suggested model statistical metrics revealed that, considering the wide range of size, mixing state, and AOD in tandem across all physically realistic possibilities improves TOA forcing compared to AOD alone.

METHODS

AERONET observations

AERONET offers long-term, continuous, and accessible observations of columnar aerosol optical, radiative, and microphysical properties from its direct and inversion products^{92–94}. The AOD product used in this work is based on direct sun, aureole and sky radiance measurements at multiple wavelengths from 340 to 1640 nm, and has been carefully characterized by many studies including^{93,95}. The SSA product used in this work is obtained from an inversion derived from sky radiance measurements, and has been shown to be valid under moderately and heavily polluted conditions ($AOD > 0.4$) both in China and in South Asia by^{29,96,97}.

This work specifically uses all points AERONET AOD at 7 different wavelength (340, 380, 440, 500, 675, 870, 1020 nm), water vapor column (WVC) and ozone column (O_3) based on the version 3 direct sun algorithm. The all points SSA is obtained at 440, 675, 870, and 1020 nm based on the version 3 inversion algorithm, which works well when the AOD at 440 nm is larger than 0.4. This study utilizes the complete set of available observations from two specific locations: Lumbini (27.49°N, 83.28°E, 110 m) in southern Nepal, a densely populated region affected by both local and transboundary aerosol loading, and Taihu (31.42°N, 120.21°E, 20 m), a site partially situated in Wuxi, China, in the middle of Tai Lake surrounded by economically active areas such as Shanghai, Suzhou, Nanjing, and Hangzhou. The datasets for Lumbini and Taihu consist of 340 and 483 days of data, respectively. These stations are selected as they are both located in moderately polluted regions, are representative of the wider Northern South Asian Plains and the wider Yangtze River Delta Region, and have many years of data and therefore have observations spanning considerable natural, climatic, and policy environments.

MIE model

The optical behavior of radiation interacting with spherical particles of a size similar to the wavelength is described by the Mie theory. Each particle has real and imaginary components of their dielectric constants respectively representing the dephasing or extinction loss by the particle (imaginary), which is physically represented by absorption, and the resonance wavelength or the polarizability (real part), which is physically represented by scattering or change in polarization. In the real atmosphere, the columnar radiative measurements and products from AERONET are linked with the presumed chemical, physical, and mixing characteristics of the particles via different optical, size, and layering assumptions on a particle-by-particle basis in accordance with and then vertically integrated. This modeling approach has been used in previous works to compute aerosol optical properties over different regions of the globe based on surface observations or fixed-point upward looking remote sensing platforms (for, e.g., refs. ^{98–100}).

To explore the impact of particle size and mixing state on DRF, this work assumes a particle structure characterized by core/shell configuration. The MIE model is subsequently used to calculate

the optical properties over a range of BC cores (50–500 nm) with refractive index $2.0 + 1.0i$ ¹⁰¹ and sulfate (SUL) shells (10–800 nm) with refractive index $1.52 - 5 \times 10^{-4}i$ ¹⁰², which are in turn used to discern core and shell particle species in the model. These results have been found to be a reasonable representation of actual conditions observed in China and South Asia^{81,82}, and are able to match results observed in regions undergoing rapid development and changes in their aerosol emissions and characterizations, changes in urbanization, impacts of biomass burning, and which are influenced by in situ processing. Overall, this work is representative of conditions found throughout China and the developing world^{4,103,104}.

The MIE model outputs scattering coefficient (Q_{scat}), absorption coefficient (Q_{abs}), and ASY parameters for all combinations of BC core and refractive shell size. All possible combination of sizes of core ranging from 50 to 500 nm and a sulfate shell ranging from 10 to 800 nm with a step size of 10 nm are computed. The Q_{scat} and Q_{abs} of the resulting distribution of parameters are used to compute the SSA on a day-to-day basis. To identify and retain the subset of size combinations that are consistent with the AERONET observations at each site on each day, this work adopts a method from set theory. Specifically, the subset of solutions of core size and shell size and resulting computed SSA are required to be consistent with the AERONET SSA observations at each of the four wavebands that SSA is provided from AERONET. This initial step involves using the all point SSA data from AERONET and determining the maximum and minimum values of SSA each day for each of the four available wavebands (440, 675, 870, 1020 nm). This range between the maximum ($SSA_{max,i}$) and minimum ($SSA_{min,i}$) values is used to bind the possible SSA values computed via the MIE model on that day (i) at that site. In the case of a single observation, or a range of observations smaller than the SSA retrieval uncertainty of 0.03, a minimum range of 0.03 is applied. This boundary conditions are consistently imposed on all four wavebands on a daily basis. The final set of aerosol sizes which are considered possible must simultaneously be a solution set of the SSA across all four wavebands. This is done by taking the logical union across the subset of sizes for both core and shell. The net size solution is the intersection across all of the four independent wavelength solutions following refs. ^{105,106}, i.e., only the set of core and shell sizes that exist in all four waveband solution spaces are utilized. Finally, the day to day set of all combinations of retained core and shell sizes are then used to run the MIE model in a forward manner, to compute the sets of optical properties also at 340 nm, 380 nm and 500 nm. All these wavebands are specifically used by AERONET for direct observations, and by combining the computed SSA and ASY distributions at these wavebands, they can be subsequently used in the radiative transfer modeling, to compute the radiative forcing.

Modeling aerosol direct radiative forcing

The Santa Barbara DISORT Atmospheric Radiative Transfer (SBDART) model¹⁰⁷ is used in this work (source: <https://github.com/paulricchiuzzi/SBDART>) to compute the atmospheric irradiance with and without the effect of aerosols. Since the majority of solar energy is observed in the range from 0.25 to 4.0 μm , this work subsequently only focuses on this region of the spectrum. To compute the irradiance, SBDART requires column AOD, water vapor, surface spectral albedo and surface ozone (from AERONET), SSA and ASY (from the MIE model), temperature, pressure, and ozone profile at different pressure levels (from ERA-5 reanalysis <https://cds.climate.copernicus.eu/cdsapp#!/dataset/reanalysis-era5-pressure-levels?tab=form>). SBDART then calculates the aerosol DRF using set of Eq. (1)–(5) as demonstrated in

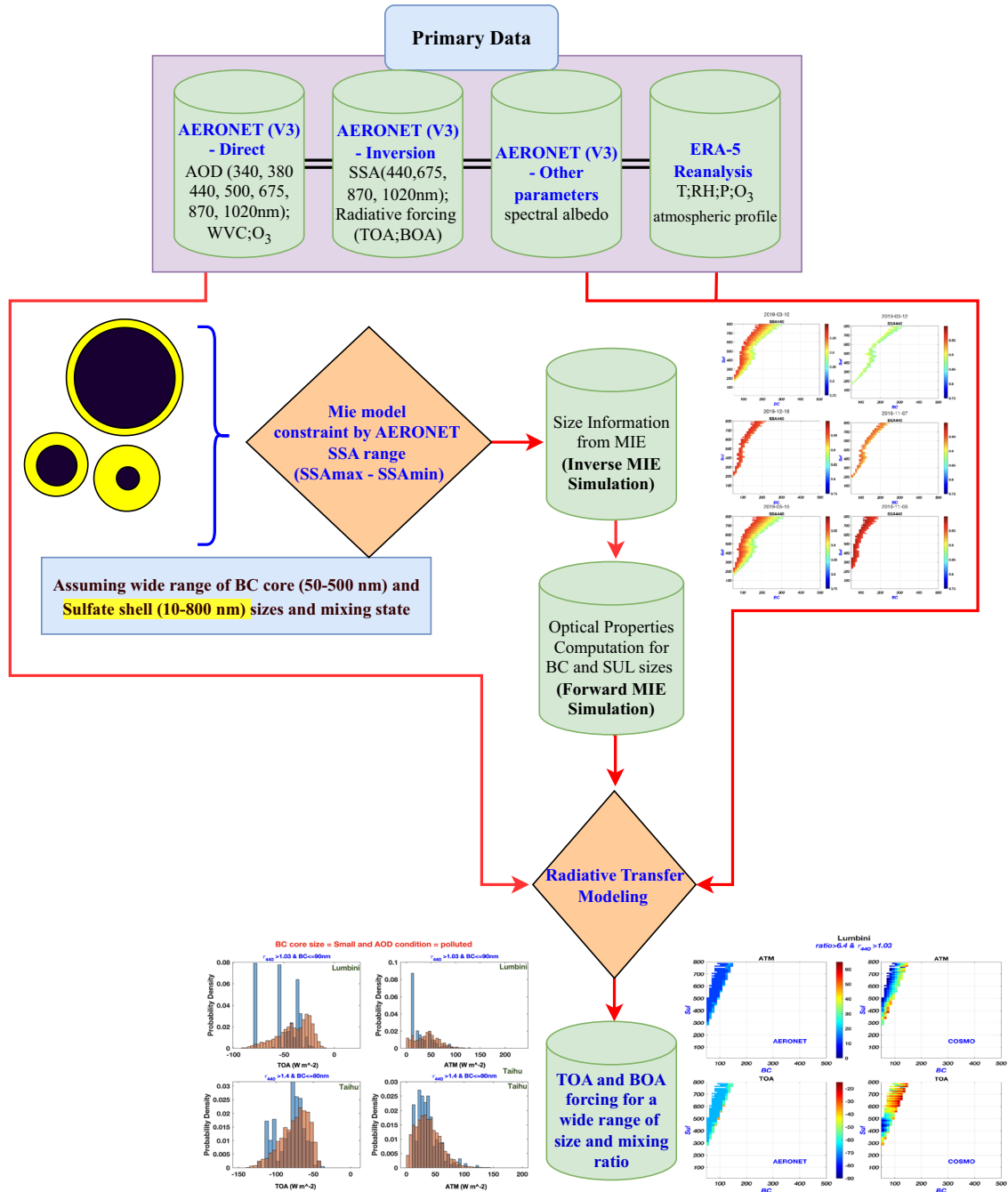


Fig. 5 Quantifying aerosol radiative forcing using a sequence of MIE inversion and forward modeling. The schematic overview of the methods used herein describes the process by which direct and inversion AERONET products and MIE models are used to constrain the BC core and shell sizes and resulting optical properties, which in turn are later used to drive the radiative transfer model across all solar and terrestrial wavelengths.

refs. 108,109

$$F_{\text{net, TOP}} = F_{\text{TOP}}^{\downarrow} - F_{\text{TOP}}^{\uparrow} \quad (1)$$

$$F_{\text{net, SUR}} = F_{\text{SUR}}^{\downarrow} - F_{\text{SUR}}^{\uparrow} \quad (2)$$

$$\text{TOA} = F_{\text{net, TOA}}^a - F_{\text{net, TOA}}^{\text{wa}} \quad (3)$$

$$\text{BOA} = F_{\text{net, BOA}}^a - F_{\text{net, BOA}}^{\text{wa}} \quad (4)$$

$$\text{ATM} = \text{TOA} - \text{BOA} \quad (5)$$

where F^{\uparrow} and F^{\downarrow} [W m^{-2}] are the respective upward and downward irradiances calculated at the top of the atmosphere [TOP] (Eq. (1)) and the surface [SUR] (Eq. (2)). From these values, TOA [W m^{-2}] and the surface atmospheric forcing (BOA) [W m^{-2}] are calculated respectively as the difference between $F_{\text{net, TOA}}^a$ (with aerosol) and $F_{\text{net, TOA}}^{\text{wa}}$ (without aerosol) and between $F_{\text{net, BOA}}^a$ (with aerosol) and $F_{\text{net, BOA}}^{\text{wa}}$ (without aerosol), respectively, on a diurnal basis following (Eq. (3)) and (Eq. (4)). ATM [W m^{-2}] is finally calculated as the difference between TOA and BOA (Eq. (5)).

An overview of the methods and approach used in this paper are given in Fig. 5.

Statistical techniques and classification

This study generates a day-to-day probabilistic set of all possible solutions of BC core size and particle shell size. This set of solutions is then used to compute the column optical properties at different wavelengths used in AERONET measurements, as well as those required to ultimately run the radiative transfer code and produce the TOA and ATM forcing. Independent comparisons have been made with size resolved aerosol core and shell measurements both on the ground in Beijing and on an aircraft platform over Seoul¹⁰⁵. The relationships are therefore identified between the aerosol size and mixing state parameters, AOD, and radiative forcing over different ranges of BC size, mixing state, and AOD, with the goal of providing a probabilistic range of the DRF of BC, identifying any biases associated with the DRF of BC, and developing a simplified and rapid procedure by which global models and analyses of BC DRF can apply the enhanced absorption effects of BC calculated herein, without needing to incorporate costly MIE models and detailed radiative forcing calculations, which otherwise do not include the effects observed in this work, or do so only using a mass-based or AOD based correction factor.

Categorizations have been made to robustly separate the resulting TOA and ATM as a function of the probabilistic distribution of the size, mixing state and AOD. Since in both sites the solution space has more than 9000 solutions for Lumbini and more than 20000 solutions for Taihu, it is sufficiently robust to divide the dataset into percentiles. In this work PDFs are developed and data is cutoff at the 25th, 50th, 75th (and in some cases 95th) percentiles as a function of (a) BCsize, (b) ratio of total size to BC size (BCsize+SULsize)/BCsize, and AOD at 440 nm, with the resulting values displayed in Table S4. In this work when using the AOD as the cutoff condition, the data below the 25th percentile is classified as clean, from the 25th to 50th percentile is classified as moderately clean, from the 50th to 75th percentile is classified as fairly polluted, and above the 75th percentile is classified as polluted, and above the 95th percentile is referred to as extremely polluted. Similar labels for BC size are, respectively, referred to as small, medium, moderately big, big, and extremely big. Similar labels for coating size (which is a proxy of chemical age and hence atmospheric in situ lifetime) are referred to as barely coated, moderately coated, substantially coated, heavily coated, and extremely heavily coated, respectively.

DATA AVAILABILITY

All underlying data herein are available for community access at <https://doi.org/10.6084/m9.figshare.23557461>.

CODE AVAILABILITY

Example code written in MATLAB for computing the aerosol optical properties are provided in <https://doi.org/10.6084/m9.figshare.23557461>. The radiative transfer code is sourced from <https://github.com/paulricchiazzi/SBDART>. The MIE model code is prepared based on Mätzler, C. (2002). MATLAB functions for Mie scattering and absorption, version2 (<https://omlc.org/software/mie/maetzlermie/Maetzler2002.pdf>). Detailed codes will be made available upon request by contacting the corresponding author or the lead author.

Received: 13 July 2023; Accepted: 3 November 2023;

Published online: 18 November 2023

REFERENCES

- Ramanathan, V. et al. Atmospheric brown clouds: impacts on South Asian climate and hydrological cycle. *Proc. Natl Acad. Sci. USA* **102**, 5326–5333 (2005).
- Bond, T. C. et al. Bounding the role of black carbon in the climate system: a scientific assessment. *J. Geophys. Res. Atmos.* **118**, 5380–5552 (2013).
- Okoye, C. O., Jones, I., Zhu, M. & Zhang, D. Manufacturing of carbon black from spent tyre pyrolysis oil – a literature review. *J. Clean. Prod.* **279**, 123336 (2021).
- Cohen, J. B. & Wang, C. Estimating global black carbon emissions using a top-down Kalman Filter approach. *J. Geophys. Res. Atmos.* **119**, 307–323 (2014).
- Wang, C. A modeling study on the climate impacts of black carbon aerosols. *J. Geophys. Res. Atmos.* **109**, D03106 (2004).
- Lau, K.-M. & Kim, K.-M. Observational relationships between aerosol and Asian monsoon rainfall, and circulation. *Geophys. Res. Lett.* **33**, L21810 (2006).
- Hansen, J., Sato, M. & Ruedy, R. Radiative forcing and climate response. *J. Geophys. Res. Atmos.* **102**, 6831–6864 (1997).
- Ramanathan, V., Crutzen, P. J., Kiehl, J. T. & Rosenfeld, D. Aerosols, climate, and the hydrological cycle. *Science* **294**, 2119–2124 (2001).
- Lohmann, U. & Feichter, J. Global indirect aerosol effects: a review. *Atmos. Chem. Phys.* **5**, 715–737 (2005).
- Takahashi, H. G., Watanabe, S., Nakata, M. & Takemura, T. Response of the atmospheric hydrological cycle over the tropical Asian monsoon regions to anthropogenic aerosols and its seasonality. *Prog. Earth Planet. Sci.* **5**, 44 (2018).
- Samsat, B. H. Aerosol absorption has an underappreciated role in historical precipitation change. *Commun. Earth Environ.* **3**, 242 (2022).
- Cohen, J. B., Prinn, R. G. & Wang, C. The impact of detailed urban-scale processing on the composition, distribution, and radiative forcing of anthropogenic aerosols. *Geophys. Res. Lett.* **38**, L15802 (2011).
- Grandey, B. S. & Wang, C. Background conditions influence the estimated cloud radiative effects of anthropogenic aerosol emissions from different source. *Reg. J. Geophys. Res. Atmos.* **124**, 2276–2295 (2019).
- Chung, S. H. Climate response of direct radiative forcing of anthropogenic black carbon. *J. Geophys. Res.* **110**, D11102 (2005).
- Boucher, O. et al. In *Climate Change 2013 the Physical Science Basis: Working Group I Contribution to the Fifth Assessment Report of the Intergovernmental Panel on Climate Change* 5th edn (eds Stocker, T. F. et al.) 571–658 (Cambridge Univ. Press, 2013).
- Tegen, I., Lacis, A. A. & Fung, I. The influence on climate forcing of mineral aerosols from disturbed soils. *Nature* **380**, 419–422 (1996).
- Westervelt, D. M., Horowitz, L. W., Naik, V., Golaz, J.-C. & Mauzerall, D. L. Radiative forcing and climate response to projected 21st century aerosol decreases. *Atmos. Chem. Phys.* **15**, 12681–12703 (2015).
- Solomon, S., Qin, D., Manning, M., Averyt, K. & Marquis, M. In *Climate Change 2007: The Physical Science Basis: Working group I contribution to the fourth assessment report of the IPCC* 4th edn, Vol.1 (Cambridge Univ. Press, 2007).
- Babu, S. S., Satheesh, S. K. & Moorthy, K. K. Aerosol radiative forcing due to enhanced black carbon at an urban site in India. *Geophys. Res. Lett.* **29**, 27–1–27–4 (2002).
- Zhuang, B. L., Liu, L., Shen, F. H., Wang, T. J. & Han, Y. Semidirect radiative forcing of internal mixed black carbon cloud droplet and its regional climatic effect over China. *J. Geophys. Res.* **115**, D00K19 (2010).
- Zhang, X. et al. Direct radiative forcing induced by light-absorbing aerosols in different climate regions over East Asia. *J. Geophys. Res. Atmos.* **125**, e2020JD033387 (2020).
- Ramachandran, S., Srivastava, R., Kedia, S. & Rajesh, T. A. Contribution of natural and anthropogenic aerosols to optical properties and radiative effects over an urban location. *Environ. Res. Lett.* **7**, 034028 (2012).
- Yu, F., Luo, G. & Ma, X. Regional and global modeling of aerosol optical properties with a size, composition, and mixing state resolved particle microphysics model. *Atmos. Chem. Phys.* **12**, 5719–5736 (2012).
- Willis, M. D. et al. Quantification of black carbon mixing state from traffic: implications for aerosol optical properties. *Atmos. Chem. Phys.* **16**, 4693–4706 (2016).
- Oshima, N., Koike, M., Zhang, Y. & Kondo, Y. Aging of black carbon in outflow from anthropogenic sources using a mixing state resolved model: 2. Aerosol optical properties and cloud condensation nuclei activities. *J. Geophys. Res.* **114**, D18202 (2009).
- Tuccella, P., Curci, G., Pitari, G., Lee, S. & Jo, D. S. Direct radiative effect of absorbing aerosols: sensitivity to mixing state, brown carbon, and soil dust refractive index and shape. *J. Geophys. Res. Atmos.* **125**, e2020JD032901 (2020).
- Chung, C. E. Aerosol Direct Radiative Forcing: A Review. In *Atmospheric Aerosols - Regional Characteristics - Chemistry and Physics* (ed. Abdul-Razzak, H.), 379–394 (IntechOpen, 2012).
- Jethva, H., Torres, O. & Ahn, C. Global assessment of OMI aerosol single-scattering albedo using ground-based AERONET inversion. *J. Geophys. Res. Atmos.* **119**, 9020–9040 (2014).
- Dubovik, O. & King, M. D. A flexible inversion algorithm for retrieval of aerosol optical properties from Sun and sky radiance measurements. *J. Geophys. Res. Atmos.* **105**, 20673–20696 (2000).

30. Kayetha, V., Torres, O. & Jethva, H. Retrieval of UV-visible aerosol absorption using AERONET and OMI-MODIS synergy: spatial and temporal variability across major aerosol environments. *Atmos. Meas. Tech.* **15**, 845–877 (2022).
31. Andreae, M. O. & Gelencsér, A. Black carbon or brown carbon? The nature of light-absorbing carbonaceous aerosols. *Atmos. Chem. Phys.* **6**, 3131–3148 (2006).
32. Kahnert, M., Nousiainen, T. & Lindqvist, H. Models for integrated and differential scattering optical properties of encapsulated light absorbing carbon aggregates. *Opt. Express* **21**, 7974 (2013).
33. Péré, J. C., Mallet, M., Bessagnet, B. & Pont, V. Evidence of the aerosol core-shell mixing state over Europe during the heat wave of summer 2003 by using CHIMERE simulations and AERONET inversions. *Geophys. Res. Lett.* **36**, L09807 (2009).
34. Liu, D. et al. Black-carbon absorption enhancement in the atmosphere determined by particle mixing state. *Nat. Geosci.* **10**, 184–188 (2017).
35. Peng, J. et al. Markedly enhanced absorption and direct radiative forcing of black carbon under polluted urban environments. *Proc. Natl Acad. Sci. USA* **113**, 4266–4271 (2016).
36. Zamora, M. L. et al. Wintertime aerosol properties in Beijing. *Atmos. Chem. Phys.* **19**, 14329–14338 (2019).
37. Dubovik, O. et al. Variability of absorption and optical properties of key aerosol types observed in worldwide locations. *J. Atmos. Sci.* **59**, 590–608 (2002).
38. Curci, G. et al. Uncertainties of simulated aerosol optical properties induced by assumptions on aerosol physical and chemical properties: an AQMEII-2 perspective. *Atmos. Environ.* **115**, 541–552 (2015).
39. Babu, S. S. & Moorthy, K. K. Anthropogenic impact on aerosol black carbon mass concentration at a tropical coastal station: a case study. *Curr. Sci.* **81**, 1208–1214 (2001).
40. Sand, M. et al. Aerosol absorption in global models from AeroCom phase III. *Atmos. Chem. Phys.* **21**, 15929–15947 (2021).
41. Romshoo, B. et al. Importance of size representation and morphology in modelling optical properties of black carbon: comparison between laboratory measurements and model simulations. *Atmos. Meas. Tech.* **15**, 6965–6989 (2022).
42. Wang, Y. et al. Constructing shapes and mixing structures of black carbon particles with applications to optical calculations. *J. Geophys. Res. Atmos.* **126**, e2021JD035140 (2021).
43. Kodros, J. K. et al. Size-resolved mixing state of black carbon in the Canadian high Arctic and implications for simulated direct radiative effect. *Atmos. Chem. Phys.* **18**, 11345–11361 (2018).
44. Zanatta, M. et al. Effects of mixing state on optical and radiative properties of black carbon in the European Arctic. *Atmos. Chem. Phys.* **18**, 14037–14057 (2018).
45. Matsui, H., Hamilton, D. S. & Mahowald, N. M. Black carbon radiative effects highly sensitive to emitted particle size when resolving mixing-state diversity. *Nat. Commun.* **9**, 3446 (2018).
46. Matsui, H. et al. Development and validation of a black carbon mixing state resolved three-dimensional model: aging processes and radiative impact. *J. Geophys. Res. Atmos.* **118**, 2304–2326 (2013).
47. Jacobson, M. Z. Strong radiative heating due to the mixing state of black carbon in atmospheric aerosols. *Nature* **409**, 695–697 (2001).
48. Bauer, S. E. et al. MATRIX (Multiconfiguration Aerosol TRacker of mIXing state): an aerosol microphysical module for global atmospheric models. *Atmos. Chem. Phys.* **8**, 6003–6035 (2008).
49. Cohen, J. B. & Prinn, R. G. Development of a fast, urban chemistry metamodel for inclusion in global models. *Atmos. Chem. Phys.* **11**, 7629–7656 (2011).
50. He, C. et al. Microphysics-based black carbon aging in a global CTM: constraints from HIPPO observations and implications for global black carbon budget. *Atmos. Chem. Phys.* **16**, 3077–3098 (2016).
51. Liu, X. et al. Description and evaluation of a new four-mode version of the Modal Aerosol Module (MAM4) within version 5.3 of the Community Atmosphere Model. *Geosci. Model Dev.* **9**, 505–522 (2016).
52. Forster, P. et al. In *Climate Change 2021: The Physical Science Basis. Contribution of Working Group I to the Sixth Assessment Report of the Intergovernmental Panel on Climate Change* 2nd edn (eds Masson-Delmotte, V. et al.) 923–1054 (Cambridge Univ. Press, 2021).
53. Chen, C. et al. Multi-angular polarimetric remote sensing to pinpoint global aerosol absorption and direct radiative forcing. *Nat. Commun.* **13**, 7459 (2022).
54. Kelesidis, G. A., Neubauer, D., Fan, L.-S., Lohmann, U. & Pratsinis, S. E. Enhanced light absorption and radiative forcing by black carbon agglomerates. *Environ. Sci. Technol.* **56**, 8610–8618 (2022).
55. Ramachandran, S., Rupakheti, M., Cherian, R. & Lawrence, M. G. Aerosols heat up the Himalayan climate. *Sci. Total Environ.* **894**, 164733 (2023).
56. Szopa, S. et al. Short-lived climate forcers. In *AGU Fall Meeting Abstracts*, Vol. 2021 U13B-06 (AGU, 2021).
57. Ching, J., Riemer, N. & West, M. Black carbon mixing state impacts on cloud microphysical properties: effects of aerosol plume and environmental conditions. *J. Geophys. Res. Atmos.* **121**, 5990–6013 (2016).
58. Chen, D., Liao, H., Yang, Y., Chen, L. & Wang, H. Simulated aging processes of black carbon and its impact during a severe winter haze event in the Beijing-Tianjin-Hebei region. *Sci. Total Environ.* **755**, 142712 (2021).
59. Gao, M. et al. Reduced light absorption of black carbon (BC) and its influence on BC-boundary-layer interactions during “APEC Blue”. *Atmos. Chem. Phys.* **21**, 11405–11421 (2021).
60. Grandey, B. S. et al. Effective radiative forcing in the aerosol-climate model CAM5.3-MARC-ARG. *Atmos. Chem. Phys.* **18**, 15783–15810 (2018).
61. Williams, A. I. L., Stier, P., Dagan, G. & Watson-Parris, D. Strong control of effective radiative forcing by the spatial pattern of absorbing aerosol. *Nat. Clim. Chang.* **12**, 735–742 (2022).
62. Watson-Parris, D. & Smith, C. J. Large uncertainty in future warming due to aerosol forcing. *Nat. Clim. Chang.* **12**, 1111–1113 (2022).
63. Zhang, X., Li, X., Chen, D., Cui, H. & Ge, Q. Overestimated climate warming and climate variability due to spatially homogeneous CO₂ in climate modeling over the Northern Hemisphere since the mid-19th century. *Sci. Rep.* **9**, 17426 (2019).
64. Vautard, R., Beekmann, M., Desplat, J., Hodzic, A. & Morel, S. Air quality in Europe during the summer of 2003 as a prototype of air quality in a warmer climate. *Comptes Rendus Geosci.* **339**, 747–763 (2007).
65. Reddington, C. L. et al. Primary versus secondary contributions to particle number concentrations in the European boundary layer. *Atmos. Chem. Phys.* **11**, 12007–12036 (2011).
66. Wu, Y., Cheng, T., Zheng, L. & Chen, H. Black carbon radiative forcing at TOA decreased during aging. *Sci. Rep.* **6**, 38592 (2016).
67. Ramana, M. V. et al. Warming influenced by the ratio of black carbon to sulphate and the black-carbon source. *Nat. Geosci.* **3**, 542–545 (2010).
68. Xu, Y., Bahadur, R., Zhao, C. & Ruby Leung, L. Estimating the radiative forcing of carbonaceous aerosols over California based on satellite and ground observations. *J. Geophys. Res. Atmos.* **118**, 11148–11160 (2013).
69. Liu, J. et al. Significant aerosol direct radiative effects during a pollution episode in northern China. *Geophys. Res. Lett.* **34**, L19803 (2007).
70. Rupakheti, D. et al. Observation of optical properties and sources of aerosols at Buddha’s birthplace, Lumbini, Nepal: environmental implications. *Environ. Sci. Pollut. Res.* **25**, 14868–14881 (2018).
71. Rupakheti, D. et al. Pre-monsoon air quality over Lumbini, a world heritage site along the Himalayan foothills. *Atmos. Chem. Phys.* **17**, 11041–11063 (2017).
72. Ramachandran, S., Rupakheti, M. & Lawrence, M. G. Black carbon dominates the aerosol absorption over the Indo-Gangetic Plain and the Himalayan foothills. *Environ. Int.* **142**, 105814 (2020).
73. Singh, P. K. et al. Variability of ambient black carbon concentration in the Central Himalaya and its assessment over the Hindu Kush Himalayan region. *Sci. Total Environ.* **858**, 160137 (2023).
74. Liu, H. et al. Mixing characteristics of refractory black carbon aerosols at an urban site in Beijing. *Atmos. Chem. Phys.* **20**, 5771–5785 (2020).
75. Yang, Y. et al. Seasonal size distribution and mixing state of black carbon aerosols in a polluted urban environment of the Yangtze River Delta region, China. *Sci. Total Environ.* **654**, 300–310 (2019).
76. Liu, X. et al. Chemical and optical properties of carbonaceous aerosols in Nanjing, eastern China: regionally transported biomass burning contribution. *Atmos. Chem. Phys.* **19**, 11213–11233 (2019).
77. Li, B. et al. Seasonal variation of urban carbonaceous aerosols in a typical city Nanjing in Yangtze River Delta, China. *Atmos. Environ.* **106**, 223–231 (2015).
78. Matsui, H. Black carbon simulations using a size- and mixing-state-resolved three-dimensional model: 1. Radiative effects and their uncertainties. *J. Geophys. Res. Atmos.* **121**, 1793–1807 (2016).
79. Fuller, K. A., Malm, W. C. & Kreidenweis, S. M. Effects of mixing on extinction by carbonaceous particles. *J. Geophys. Res. Atmos.* **104**, 15941–15954 (1999).
80. Zhang, Y. et al. Evidence of major secondary organic aerosol contribution to lensing effect black carbon absorption enhancement. *NPJ Clim. Atmos. Sci.* **1**, 47 (2018).
81. Chin, M. et al. Multi-decadal aerosol variations from 1980 to 2009: a perspective from observations and a global model. *Atmos. Chem. Phys.* **14**, 3657–3690 (2014).
82. Schmidt, G. A. et al. Configuration and assessment of the GISS ModelE2 contributions to the CMIP5 archive. *J. Adv. Model. Earth Syst.* **6**, 141–184 (2014).
83. Bond, T. C. & Bergstrom, R. W. Light absorption by carbonaceous particles: an investigative review. *Aerosol Sci. Technol.* **40**, 27–67 (2006).
84. Eck, T. F. et al. Optical properties of boreal region biomass burning aerosols in central Alaska and seasonal variation of aerosol optical depth at an Arctic coastal site. *J. Geophys. Res.* **114**, D11201 (2009).

85. AboEl-Fetouh, Y. et al. Climatological-scale analysis of intensive and semi-intensive aerosol parameters derived from AERONET retrievals over the Arctic. *J. Geophys. Res. Atmos.* **125**, e2020JD033340 (2020).
86. O'Neill, N. T. et al. Relationship between the sub-micron fraction (SMF) and fine-mode fraction (FMF) in the context of AERONET retrievals. *Atmos. Meas. Tech.* **16**, 1103–1120 (2023).
87. Zhao, G. et al. Mixing state of black carbon at different atmospheres in north and southwest China. *Atmos. Chem. Phys.* **22**, 10861–10873 (2022).
88. Cho, C. et al. Light-absorption enhancement of black carbon in the Asian outflow inferred from airborne SP2 and in-situ measurements during KORUS-AQ. *Sci. Total Environ.* **773**, 145531 (2021).
89. Freychet, N., Hegerl, G., Mitchell, D. & Collins, M. Future changes in the frequency of temperature extremes may be underestimated in tropical and sub-tropical regions. *Commun. Earth Environ.* **2**, 28 (2021).
90. Mallet, M. et al. Climate models generally underrepresent the warming by Central Africa biomass-burning aerosols over the Southeast Atlantic. *Sci. Adv.* **7**, eabc1067 (2021).
91. Rantanen, M. et al. The Arctic has warmed nearly four times faster than the globe since 1979. *Commun. Earth Environ.* **3**, 168 (2022).
92. Khor, W. Y. et al. Comparison of Aerosol optical depth (AOD) derived from AERONET sunphotometer and Lidar system. *IOP Conf. Ser. Earth Environ. Sci.* **20**, 12058 (2014).
93. Eck, T. F. et al. Wavelength dependence of the optical depth of biomass burning, urban, and desert dust aerosols. *J. Geophys. Res. Atmos.* **104**, 31333–31349 (1999).
94. Holben, B. N. et al. AERONET—a federated instrument network and data archive for aerosol characterization. *Remote Sens. Environ.* **66**, 1–16 (1998).
95. Smirnov, A., Holben, B. N., Eck, T. F., Dubovik, O. & Slutsker, I. Cloud-screening and quality control algorithms for the AERONET database. *Remote Sens. Environ.* **73**, 337–349 (2000).
96. Dubovik, O. et al. Accuracy assessments of aerosol optical properties retrieved from Aerosol Robotic Network (AERONET) Sun and sky radiance measurements. *J. Geophys. Res. Atmos.* **105**, 9791–9806 (2000).
97. Dubovik, O. et al. Application of spheroid models to account for aerosol particle nonsphericity in remote sensing of desert dust. *J. Geophys. Res.* **111**, D11208 (2006).
98. Majdzadeh, M. et al. Development of aerosol optical properties for improving the MESSy photolysis module in the GEM-MACH v2.4 air quality model and application for calculating photolysis rates in a biomass burning plume. *Geosci. Model Dev.* **15**, 219–249 (2022).
99. Hudson, P. K., Gibson, E. R., Young, M. A., Kleiber, P. D. & Grassian, V. H. A newly designed and constructed instrument for coupled infrared extinction and size distribution measurements of aerosols. *Aerosol Sci. Technol.* **41**, 701–710 (2007).
100. Chylek, P. et al. Mie scattering captures observed optical properties of ambient biomass burning plumes assuming uniform black, brown, and organic carbon mixtures. *J. Geophys. Res. Atmos.* **124**, 11406–11427 (2019).
101. Schuster, G. L. Inferring black carbon content and specific absorption from Aerosol Robotic Network (AERONET) aerosol retrievals. *J. Geophys. Res.* **110**, D10517 (2005).
102. Aouizerats, B. et al. Development of an online radiative module for the computation of aerosol optical properties in 3-D atmospheric models: validation during the EUCAARI campaign. *Geosci. Model Dev.* **3**, 553–564 (2010).
103. May, A. A. et al. Observations and analysis of organic aerosol evolution in some prescribed fire smoke plumes. *Atmos. Chem. Phys.* **15**, 6323–6335 (2015).
104. Song, C. H. & Carmichael, G. R. The aging process of naturally emitted aerosol (sea-salt and mineral aerosol) during long range transport. *Atmos. Environ.* **33**, 2203–2218 (1999).
105. Wang, X., Cohen, J. B. & Wang, S. Combining multi-wavelength AERONET SSA retrievals with a MIE model to quantify the size of absorbing aerosols and the in-situ lifetime of sulfate. *Earth Space Sci. Open Arch.* **30**, e2022EA001724 (2022).
106. Wang, S., Wang, X., Cohen, J. B. & Qin, K. Inferring polluted Asian absorbing aerosol properties using decadal scale AERONET measurements and a MIE model. *Geophys. Res. Lett.* **48**, e2021GL094300 (2021).
107. Ricchiazzi, P., Yang, S., Gautier, C. & Sowle, D. SBDART: a research and teaching software tool for plane-parallel radiative transfer in the Earth's atmosphere. *Bull. Am. Meteorol. Soc.* **79**, 2101–2114 (1998).
108. Wang, Y. et al. Retrieval of gridded aerosol direct radiative forcing based on multiplatform datasets. *Atmos. Meas. Tech.* **13**, 575–592 (2020).
109. Patel, P. N., Dumka, U. C., Babu, K. N. & Mathur, A. K. Aerosol characterization and radiative properties over Kavaratti, a remote island in southern Arabian Sea from the period of observations. *Sci. Total Environ.* **599–600**, 165–180 (2017).

ACKNOWLEDGEMENTS

We would like to acknowledge the PIs of the AERONET instruments for providing the remote sensing measurements (<https://aeronet.gsfc.nasa.gov>). The work was supported by the Chinese National Natural Science Foundation under Grant 42075147 and Grant 41975041, the Fundamental Research Funds for the Central Universities under Grant 2023KYJD1003, and the China Scholarship Council 2021GXZ007839.

AUTHOR CONTRIBUTIONS

P.T.: conceptualization, formal analysis, investigation, methodology, software, validation, visualization, writing—original draft, writing—review and editing. J.B.C.: conceptualization, funding acquisition, investigation, methodology, project administration, resources, supervision, validation, writing—original draft, writing—review and editing. X.W. and S.W.: software, writing—review and editing. K.Q.: writing—review and editing.

COMPETING INTERESTS

The authors declare no competing interests.

ADDITIONAL INFORMATION

Supplementary information The online version contains supplementary material available at <https://doi.org/10.1038/s41612-023-00520-1>.

Correspondence and requests for materials should be addressed to Jason Blake Cohen.

Reprints and permission information is available at <http://www.nature.com/reprints>

Publisher's note Springer Nature remains neutral with regard to jurisdictional claims in published maps and institutional affiliations.



Open Access This article is licensed under a Creative Commons Attribution 4.0 International License, which permits use, sharing, adaptation, distribution and reproduction in any medium or format, as long as you give appropriate credit to the original author(s) and the source, provide a link to the Creative Commons license, and indicate if changes were made. The images or other third party material in this article are included in the article's Creative Commons license, unless indicated otherwise in a credit line to the material. If material is not included in the article's Creative Commons license and your intended use is not permitted by statutory regulation or exceeds the permitted use, you will need to obtain permission directly from the copyright holder. To view a copy of this license, visit <http://creativecommons.org/licenses/by/4.0/>.

© The Author(s) 2023